High-resolution Biological Net Community Production in the Pacific-influenced Arctic: A Multi-Method Comparison

Haley Cynar[1], Lauren W. Juranek[1], Calvin W. Mordy[2,3], David Strausz[2,3], Shaun Bell[3]

[1] College of Earth, Ocean, and Atmospheric Sciences, Oregon State University, Corvallis, USA

[2] Cooperative Institute for Climate, Ocean, and Ecosystem Studies, University of Washington, Seattle, USA

[3] Pacific Marine Environmental Laboratory, National Oceanic and Atmospheric Administration, Seattle, USA

ORCID:

(HC) https://orcid.org/0000-0003-0609-5226

(LWJ) https://orcid.org/0000-0002-4922-8263

(CWM) https://orcid.org/0000-0002-3674-7072

Correspondence: cynarh@oregonstate.edu

Abstract

Spatial and temporal patterns of primary productivity in the Arctic are expected to change with warming-associated changes in ice cover and stratification, yet productivity measurements are historically spatially and temporally limited. An established method to estimate net community production (NCP) rates involves measurement of dissolved oxygen/argon gas ratios (O_2/Ar) from a vessel's underway seawater system. An emerging method that may provide comparable NCP estimates involves measurement of oxygen/nitrogen ratios (O_2/N_2) with a gas tension device (GTD) and optode. The GTD/optode combo has several advantages: it is small, inexpensive, and suitable for autonomous deployments; however, the dissimilarity in solubility between O_2 and N_2 makes this tracer pair less favorable than O_2/Ar. We conducted a side-by-side comparison of a GTD and EIMS during the 2019 Arctic Integrated Ecosystem Survey OS1901-L1 in the Pacific Arctic. NCP from these two approaches were generally consistent throughout this cruise, with median NCP from O_2/Ar and O_2/N_2 of 7.33 ± 2.43 and 9.43 ± 2.73 mmol O_2 m^{-2} day^{-1} in comparable regions, respectively. While O_2/Ar and O_2/N_2 tracked each other in patterns, there were small deviations due to different sensitivities to physical drivers, which included a section in the Bering Strait where wind induced bubbles were the primary driver, followed by a period where both temperature and wind were thought to drive the differences between O_2/Ar and O_2/N_2. These results suggest that the GTD/optode can be used to enhance spatial and temporal coverage of NCP measurements. However, the GTD/optode approach is reliant on well-calibrated oxygen observations, a potential challenge if the GTD/optode is autonomously deployed. Uncertainty in the GTD/optode approach makes it well-suited to regions with strong gradients in NCP, while regions near equilibrium may result in unacceptably high uncertainty.

Introduction

The Arctic Ocean is changing at an unprecedented rate: the thirteen lowest minimum sea ice extents in the satellite record have all occurred between 2007 and 2020, while the trend in September sea ice extent has been declining by 13.3% per decade over the period 1979-2014, relative to the mean September sea ice extent from 1981-2010 (Serreze and Stroeve 2015; Stroeve and Meier 2018; Andersen et al. 2020). In some of the most impacted regions of the Arctic Ocean, including the Chukchi and western Beaufort seas, the ice season duration has been declining by an average of 2.8 days per year from 1979/1980 to 2010/2011 (Stammerjohn et al. 2012). This rapid decline in sea ice impacts the physical environment in many ways: increased exchange of heat and gases (CO_2) across the air-sea boundary (Anderson and Kaltin 2001; Carmack et al. 2015; Danielson et al. 2020; DeGrandpre et al. 2020), enhanced wind fetch across open water that results in greater waves (Thomson and Rogers 2014), and greater stratification from low-salinity meltwater (Toole et al. 2010). Stronger stratification limits vertical mixing, which in turn limits surface nutrient supply, a fundamental requirement for photosynthesis (Semiletov et al. 2004; Carmack and Wassmann 2006; Song et al. 2021).

The impact of these physical changes on primary productivity is uncertain, with hypotheses for both increasing and decreasing production based on nutrient and light availability. Remote sensing studies have indicated an increase in primary production, driven by sea ice loss and reduction in light limitation (Arrigo et al. 2008; Tremblay et al. 2011; Arrigo and van Dijken 2015), although these studies acknowledge a requirement for increased nutrient flux to maintain production. This influx of nutrients could be sustained by increased supply from adjacent subpolar seas. Nitrate replenishment is highly variable in the eastern Chukchi Sea (Mordy et al.

2020), an inflow shelf, and inflow shelves are expected to be most impacted by enhanced nutrient supply from neighboring seas (Tremblay and Gagnon 2009; Tremblay et al. 2015; Lewis et al. 2020). Alternatively, potential increases in cloud cover are expected to decrease production (Bélanger et al. 2013), while increased delivery of freshwater and dissolved constituents from terrestrial snow, ice, and permafrost melt via Arctic rivers will impact nutrients, stratification, and organic matter in coastal regions with variable results (Carmack and Wassmann 2006). Overall, a melting Arctic Ocean will alter surface light and nutrient availability on a seasonal basis, effectively controlling phytoplankton growth, and thus carbon and energy cycling in Arctic marine food webs (Grebmeier et al. 2006; Harada 2016).

While remote sensing approaches are one of the best tools for providing spatially and temporally resolved estimates of marine productivity, passive measurements (e.g. ocean color) are often limited in some seasons and regions of the Arctic due to cloud cover, especially during the late ice-free season (August-October) when physical system changes exhibit strong trends. Field-based observations of productivity are still needed to calibrate and validate remote sensing algorithms and to identify or confirm mechanisms supporting enhanced growth. Incubation-based studies (Hill and Cota 2005; Quay et al. 2012; Ducklow and Doney 2013) are the most commonly used field-based approach for constraining marine productivity, but these discrete measurements are time- and labor-intensive, have unknown uncertainties due to bottle effects, and are inevitably limited in quantity and spatial/temporal scope. Since biological production in shallow, marginal seas like the Chukchi can be dynamic, with patchy and short-lived phytoplankton blooms (Juranek et al. 2019), higher resolution methods are needed to capture sporadic and spatially-variable processes in the field.

In the last two decades, a number of studies have shown the utility of high-resolution observations of surface ocean dissolved oxygen/argon (O_2/Ar) gas ratios to constrain ocean net community production (NCP) at spatial and or temporal scales that are not accessible with traditional incubation methods (e.g., Hamme et al., 2012; Eveleth et al., 2017, Juranek et al., 2019). An important productivity metric, NCP is defined as the total community photosynthesis less both algal and heterotrophic respiration, and is considered to be a measure of the organic carbon available to be exported out of the surface ocean or consumed by higher trophic levels, with implications for the ecosystem, fisheries, carbon budgets, and climate modeling (Wassmann and Reigstad 2011).

High-resolution O_2/Ar can be obtained continuously in surface seawater using an equilibrated inlet mass spectrometer (EIMS) (Cassar et al. 2009). Since Ar is an inert gas that is not affected by biology but behaves similarly to O_2 with respect to physical forcing, it can be used to isolate the biological effects driving O_2 (Benson and Krause 1984; Craig and Hayward 1987). The ratio of biologically and physically controlled O_2 to physically controlled Ar therefore can be used to provide an estimate of net biological oxygen production (Kaiser et al. 2005). The O_2/Ar ratio is insensitive to changes in dissolved gases such as warming, cooling, and wind-driven bubble exchange and injection due to the similarity in physical properties between oxygen and argon. When O_2/Ar measurements are combined with a simple steady state mass-balance budget for the surface ocean, spatially resolved estimates of NCP can be produced (e.g., Stanley et al. 2010; Hamme et al. 2012; Eveleth et al. 2017).

Another related, but less frequently used approach for obtaining NCP is to use observations of the O_2/N_2 ratio in seawater. Similar to the case with O_2/Ar, N_2 is used to track abiotic forcing. However, while O_2 and Ar are an ideal tracer pair due to the similar solubility of these gases, the solubility of N_2 is less similar to O_2, and is impacted differently by both physical forcing (i.e., warming, cooling, and bubbles) and, at times, biological influences (i.e., nitrogen fixation and denitrification).

The O_2/N_2 method was previously described by Emerson et al. (2002), who used observations from an O_2 optode and a gas tension device (GTD) mounted on a mooring near the Hawaii Ocean Time-series study site in the subtropical North Pacific to estimate net biological oxygen production. The approach involves measuring total gas pressure as well as pO_2 in seawater with a GTD and O_2 sensor, respectively, with assumptions about less prevalent gases to estimate the amount of dissolved N_2. Because of the reliance on O_2 to calculate N_2, the approach requires accurate dissolved O_2 concentrations (Emerson et al., 2002).

GTD measurements were first tested on moorings (McNeil et al. 1995) and have since been broadly applied (Emerson et al. 2002, 2008; Weeding and Trull 2014; Trull et al. 2019), while continuous shipboard GTD measurements have also been made to estimate O_2/N_2-based net biological oxygen production (McNeil et al. 2005). Emerson et al. (2019) verified the role bubbles play in air-sea gas exchange using a GTD, an advancement which consequently enhances the use of O_2/N_2 in determining biological oxygen production. Recently, Izett and Tortell (2020) introduced a GTD and optode configuration (Pressure of In Situ Gases Instrument, or PIGI) for deployment on underway systems, with initial data collection in the northeast Pacific and Canadian Arctic oceans.

While O_2/N_2-based net biological oxygen estimates are subject to greater biases and uncertainties due to the dissimilarities in physical forcing of O_2 and N_2, there are also key advantages to the approach. The GTD/optode system is small, submersible, and low-cost, with potential for autonomous use, whereas the EIMS involves a more expensive, ship-based mass spectrometer that requires supervision.

Here, we compare underway O_2/N_2 to the more established O_2/Ar method (Stanley et al. 2010; Hamme et al. 2012; Lockwood et al. 2012; Eveleth et al. 2014) to (1) evaluate the utility of this approach for autonomous underway applications, (2) quantify spatial variability in NCP, and (3) evaluate potential physical drivers of NCP in this region of the Pacific Arctic.

Basis of O_2/Ar and O_2/N_2 approach

Biological O_2 production can be stoichiometrically related to the net inventory of organic carbon produced through the balance of community photosynthesis and respiration, i.e.: $CO_2 + H_2O \leftrightarrow$ organic matter + O_2. As is evident from this expression, net biological oxygen increases (decreases) due to photosynthesis (respiration) in a given parcel of water. However, background concentrations of O_2 in surface seawater are set by temperature- and salinity- controlled solubility (Garcia and Gordon, 1992). Therefore, small deviations from solubility equilibrium, identified by the dissolved gas saturation of oxygen in the surface ocean:

$$\Delta O_2\ (\%) = 100*([O_2]_{meas}/[O_2]_{sat} - 1) \quad (1)$$

give an indication of small deviations from solubility equilibrium that are driven by biological and physical forcing. For example, a recent water column warming of 3°C (e.g. from 10° to 13°C) without sufficient time for re-equilibration with the atmosphere would increase ΔO_2 by 6.57% due to the decrease in solubility of O_2 ($[O_2]_{sat}$) with increasing temperature. A positive gas saturation could also be driven by a source of O_2 (i.e. photosynthesis), which increases $[O_2]_{meas}$. Without an additional tracer gas, it is difficult to identify when positive ΔO_2 are driven by biological production or a combination of physical factors. By simultaneously measuring an abiotic gas such as Ar or N_2 as a tracer of physical saturation changes, the physical and biological components of the ΔO_2 signal can be parsed out. Ar has been widely used as an abiotic tracer alongside O_2 because it is inert and is physically similar to oxygen (Craig and Hayward 1987). Although N_2 has biological sources and sinks, the effect of these processes are typically assumed to be undetectable given the large N_2 background in surface measurements, making N_2 an effective tracer of physical processes (Emerson et al. 2002). With Ar and N_2 serving as proxies for physical gas saturation, the normalization of ΔO_2 relative to either gas yields a tracer of the net biological oxygen saturation (Kaiser et al., 2005).

The physical differences between N_2 and O_2 are significantly greater than those between Ar and O_2, so physical forcing (for example, warming or cooling of water masses) is expected to drive slightly different responses in O_2 and N_2, and hence the O_2/N_2 ratio will not be a perfect tracer of net biological O_2 production. Since N_2 makes up 78% of the atmosphere (Glueckauf 1951) yet is less soluble in seawater than either O_2 or Ar, the effect of bubble injection increases N_2 saturation significantly more than O_2 or Ar. The effect of temperature change on N_2, in contrast, is smaller than that of O_2 and Ar, which also biases the ratio when temperature change is observed.

To account for the physical biases of N_2, Izett et al. (2021) introduced a calculated value, N_2', which more closely approximates a physical analogue of oxygen, improving upon the approximation of net biological oxygen production based on O_2/N_2 in some regions. We explored the utility of this N_2' approach in our study region by comparing O_2 /N_2 and O_2 /N_2', with O_2 /Ar observations.

Methods

In this study, EIMS- and GTD- based estimates of NCP were obtained for a side-by-side comparison on leg 1 of the OS1901 cruise (August 1 to August 24, 2019), part of the North Pacific Research Board's Arctic Integrated Ecosystem Research Program in the Chukchi and Beaufort Seas, on R/V *Ocean Starr*. Leg 1 of the cruise embarked from Dutch Harbor, AK and ended in Nome, AK.

Dissolved O_2 measurements

An Aanderaa optode (4330F) was placed in-line with the GTD in the flowthrough seawater system, which had a nominal intake depth of 3.5 meters. The optode was calibrated from discrete samples that were collected periodically throughout the cruise (n=26), and analyzed using the Winkler method (Carpenter 1965). Upon inspection, 5 of these samples were determined to be outliers (offset >2σ from mean or were analyzed in a batch of samples that were subject to analysis error); these outliers were excluded from further analysis. Oxygen gain (Winkler O_2/optode O_2) was determined with respect to time, temperature, and oxygen concentration, where the best fit linear model of the difference in gain correction as a function of time (R_2 = 0.58) was applied to the data (Fig. S1, Supplemental Information). This time-based gain correction ranged from 1.034 to 1.051 and is described in the Supplemental Information.

EIMS-O_2/Ar

An equilibrated inlet mass spectrometer (EIMS), which consists of a quadrupole mass spectrometer (Pfeiffer PrismaPlus QMG 220) coupled to a system for separation of dissolved gases from seawater, was configured similarly to that described by Cassar et al. (2009). O_2/Ar ratios were continuously measured on surface seawater by the EIMS, where seawater passed through a 40 mesh (0.42 mm) coarse screen, followed by 100 μm and 5 μm filters before entering an overflowing cylinder in a sipper system. Seawater near the inflow of this cylinder was pumped through a contactor membrane (3M Liqui-cel MicroModule 0.75 x 1, model G569) with large surface area in which dissolved gases equilibrated. The headspace of gas in this contactor membrane was sampled by a fused silica capillary (2 m x .05 mm ID) connected to the quadrupole mass spectrometer. A changeover valve allowed outside air to be admitted for 30 minutes every 3 hours. O_2/Ar in ambient air is considered to be constant, so consistent air measurements throughout the cruise allows for calibration of the seawater O_2/Ar signal to air O_2/Ar to account for potential drift in EIMS measurements over time.

The EIMS O_2/Ar ratios were time-averaged into 2.5-minute intervals to yield measurements with average spatial resolution of ca. 0.6 km along the ship transit. EIMS-based O_2/Ar measurements are slightly lagged relative to faster response O_2 optode data due to equilibration and capillary transport time. Using a cross-correlation analysis, an EIMS-to-optode lag of 8.5 minutes was identified, and the EIMS measurements were adjusted accordingly to align with the faster response optode data. Bottle samples were collected from the underway seawater stream twice a day and analyzed via a shore-based Thermo 253 Isotope Ratio Mass Spectrometer (IRMS) as in Juranek et al. (2012). Bottle samples were used as a secondary, external accuracy check on air corrected EIMS O_2/Ar. Outliers in the bottle calibrations (offset $>3\sigma$ from mean difference) were observed in frontal regions of rapid O_2/Ar ratio change, and were excluded from comparison because small differences in sampling response time allowed for large offsets between EIMS and bottle O_2/Ar that were inconsistent with the majority of the data. Bottle and EIMS O_2/Ar data were used with paired temperature and salinity to calculate the O_2/Ar saturation (ΔO_2/Ar) as follows:

$\Delta O_2/Ar=100*[(O_2/Ar)_{meas}/(O_2/Ar)_{sat}-1]$, (2)

where $(O_2/Ar)_{sat}$ refers to the ratio of gases at saturation in seawater at 1-atm pressure of air, and O_2 and Ar solubilities are calculated according to Garcia and Gordon (1992) and Hamme and Emerson (2004), respectively. We observed a consistent, stable offset between EIMS and bottle sample $\Delta O_2/Ar$ of -1.33 % (n=34, s.e.m.=0.1%). We adjusted all EIMS data to correct for this offset. See metadata description accompanying archived data (https://doi.org/10.18739/A2319S41N) for further details.

GTD-O_2/N_2

The Pro-Oceanus miniTDGP (referred to as GTD) was installed on the flowthrough seawater system to measure total dissolved gas pressure of surface seawater throughout the cruise. This device measures the total dissolved gas pressure across a permeable membrane twice per second. The flow rate of seawater entering the GTD was about 1.2 L min^{-1}, which yielded measurements with a faster response time than the EIMS. Since this configuration was set up directly in line with the underway seawater (in contrast to the EIMS with a sipper), these measurements were subject to greater noise at times due to bubbles in the seawater line.

The GTD measures total dissolved gas pressure in seawater ($P^w_{GTD,}$) expressed as in Equation 3,

$$P^w_{GTD}= P^w_{N2} + P^w_{O2} + P^w_{H20} + P^w_{Ar} + P^w_{CO2} \quad (3)$$

where P^w_x refers to the partial pressure of dissolved N_2, O_2, water vapor, Ar, and CO_2 in seawater, respectively. This expression excludes gases with partial pressures less than 20 µatm, which Emerson et al. (2002) showed was a reasonable assumption. P^w_{Ar}, P^w_{CO2}, and P^w_{H2O} are assumed to be at equilibrium with the atmosphere, an assumption that is likely inaccurate, yet expected deviations in these gas concentrations will not strongly affect the calculation due to the small contribution of each of these gases to total dissolved gas pressure. Alternately, the saturation of Ar can be assumed to be equal to N_2 in the calculation based on roughly similar saturations from physical forcing (McNeil et al. 2005). In this study, we assume P^w_{Ar} to be in equilibrium with the atmosphere, but we investigate the impact of these assumptions in a later section (*EIMS-GTD comparison)*. The dry air mole fraction of CO_2 in the atmosphere was used in this calculation, where the monthly average pCO_2 in August 2019 at the Point Barrow, AK climate monitoring station was 400 ppm (NOAA CMDL, https://www.esrl.noaa.gov/gmd/dv/data/). The partial pressure of CO_2 and Ar were calculated based on the mole fraction of each gas in the atmosphere with the relationship in Equation 4:

$$P^a_i = X_i * (P^a - P^a_{H20}) \quad (4)$$

where P^a_i is the partial pressure of gas (i=CO_2 or Ar), X_i is the fraction of gas in a dry atmosphere, P^a is the atmospheric pressure and P^a_{H2O} is the partial pressure of water vapor in the atmosphere (Glueckauf 1951). P^w_{H2O} is assumed to be at saturation in the surface ocean and is calculated with the formula of Weiss and Price (1980). Daily atmospheric pressure (P^a) at mean sea level along the cruise track was determined from NCEP North American Regional Reanalysis (NARR) data provided by the NOAA/OAR/ESRL Physical Science Laboratory (Mesinger et al. 2006), Boulder, Colorado, USA (https://psl.noaa.gov/).

To calculate the partial pressure of dissolved oxygen, a solubility constant, α_{O2}, was calculated with units of mol kg^{-1} atm^{-1} as follows:

$$\alpha_{O2} = [O_2]_{sat} / (P^a - P^a_{H2O}) * X_{O2}$$

(5)

where the equilibrium saturation concentration of oxygen at each location, $[O_2]_{sat}$, was determined based on the equations of Garcia and Gordon (1992). As above, P^a is atmospheric pressure and P^a_{H2O} is the partial pressure of water vapor in the atmosphere (assumed to be at saturation) and X_{O2} is the mole fraction of O_2 in a dry atmosphere (Glueckauf 1951). This solubility constant, α_{O2}, was then used to calculate the partial pressure of O_2 in the water vapor-saturated headspace of the GTD as in Equation 6,

$$P^w_{O2} = [O_2]_{meas}/\alpha_{O2} \quad (6)$$

where $[O_2]_{meas}$ is the concentration of O_2 measured by the optode, in mol/kg.

The P^w_{N2} can then be calculated as (Emerson et al. 2002):

$$P^w_{N2} = P^w_{GTD} – (P^a-P^a_{H20})*(X_{Ar} + X_{CO2}) – P^w_{H20} – [O_2]_{meas}/\alpha_{O2}; \quad (7)$$

The P^w_{GTD} data were time-shifted to account for a 6.5-minute GTD-to-optode lag (determined via a cross-correlation analysis) relative to the faster response Aanderaa optode data, a response time that is slower than comparable systems (Izett and Tortell 2020) and is attributed to the low flow rate of seawater on this cruise. From P^w_{N2} and P^w_{O2} as calculated post P^w_{GTD} lag correction, measured O_2/N_2 ratios were determined.

We report O_2/N_2 here in terms of a saturation ratio comparable to Equation 2:

$$\Delta O_2/N_2\ (\%)=100*[\ (O_2/N_2)_{meas}/(O_2/N_2)_{sat}\ -1] \quad (8)$$

where $(O_2/N_2)_{sat}$ refers to the ratio of gases at saturation in equilibrium with the GTD headspace as calculated by Equation 6 or 7. The gas solubilities are calculated from Garcia and Gordon (1992) and Hamme and Emerson (2004). In calculating the O_2/N_2 ratio, a median residual filter was applied to the raw gas pressure data to remove outliers and noise due to in-line bubbles; see metadata description accompanying archived data (https://doi.org/10.18739/A2Z892G7H) for further details.

Comparison of O_2 /Ar and O_2 /N_2 data

To assess the difference between O_2/Ar and O_2/N_2 ratios, we calculate the term diff-Δ:

$$\text{diff-}\Delta\ (\%) = \Delta O_2/Ar - \Delta O_2/N_2 \qquad (9)$$

In order to calculate diff-Δ, we must first account for differences in the dynamic response of each instrument. The EIMS equilibrator uses a contactor membrane that dampens the signal due to the time required for gases to reach equilibrium across the membrane. When calculating diff-Δ, this difference in time responses between instruments creates large data artifacts due to mismatched peaks. To account for the smearing of signals within the EIMS equilibrator, a smoothed version of $\Delta O_2/N_2$ was calculated for use in comparing the two ratios. A one-sided exponential filter with an e-folding time of 7.75 minutes was applied over three time periods to the total dissolved gas pressure measurements to simulate the smoothing effect of the EIMS contactor membrane, hereafter referred to as $\Delta O_2/N_{2smoothed}$. This e-folding time was determined by Cassar et al. (2009) for a comparable EIMS configuration. After applying this filter, the gas pressure signal was aligned with the optode and averaged into 2.5 minute bins corresponding to those of O_2/Ar from the EIMS. See metadata description accompanying archived data (https://doi.org/10.18739/A2Z892G7H) for further details.

NCP calculation

Net community production (NCP) was calculated for $\Delta O_2/Ar$ and $\Delta O_2/N_2$ values by assuming a steady state balance between net biological oxygen production and air-sea gas exchange in the surface mixed layer with no horizontal advection or vertical mixing of water masses (Craig and

Hayward 1987; Kaiser et al. 2005; Hamme and Emerson 2006; Stanley et al. 2010). When there is physical transport of deeper water to the surface and mixing assumptions are invalidated it is not appropriate to calculate NCP using the steady-state balance (Teeter et al. 2018). Diagnosing potential mixing biases using only surface underway data can be challenging, but some characteristics of deeper water that may indicate vertical mixing in the region of this study include elevated salinity coupled with negative $\Delta O_2/Ar$ at the surface, since subsurface waters are typically depleted in oxygen at depth due to respiration, and their salinity is higher due to minimal influence of seasonal ice melt at depth. In this dataset, areas with both a $\Delta O_2/Ar$ less than -2% and a surface salinity greater than 32.5 (where the mean surface salinity over the cruise was 30.6, with less than 5% of measurements greater than 32.5) are assumed to be subject to vertical mixing, and are excluded from NCP calculations.

NCP based on the surface mass balance (Hendricks et al. 2004; Juranek and Quay 2005) was calculated using Equation 10 with NCP in mmol O_2 m^{-2} day^{-1}:

$$NCP=(k_{O2})(O_2)_{sat}(\Delta O_2/[X])/100, \qquad (10)$$

In Equation 10, k_{O2} is the air-sea gas exchange rate (m day^{-1}), $(O_2)_{sat}$ is the equilibrium saturation of oxygen calculated as described above (mmol m^{-3}), and $\Delta O_2/[X]$ is either $\Delta O_2/Ar$ or $\Delta O_2/N_2$ as calculated with Equation 2 or 8. The gas transfer velocity, k_{O2}, is dependent on wind speed and was calculated based on Wanninkhof (2014) using the wind speed weighting technique of Reuer et al. (2007). Three-hourly average directional components of wind speed from NCEP North American Regional Reanalysis (NARR) provided by the NOAA/OAR/ESRL PSL, Boulder, Colorado, USA were used in calculating the gridded wind speed for the 60 days prior to ship observations. (https://psl.noaa.gov/).

Variables to Assess Physical Gas Saturation

To evaluate potential variables that might corelate with differences in O_2/Ar and O_2/N_2 ratios, we compare remotely sensed wind speed and temperature to diff-Δ. The three-hour wind speed from NARR was used in calculating the maximum wind speed over the two preceding weeks, as well as the percent of wind speeds exceeding 10 m s^{-1} over prior weeks. Net temperature change was calculated as the sum of daily sea surface temperature (SST) change 14 and 30 days prior to sampling using NOAA High-resolution Blended Analysis of Daily SST and Ice data collocated with the cruise track provided by the NOAA/OAR/ESRL PSL, Boulder, Colorado, USA, from (https://psl.noaa.gov/).

N_2' Calculations

N_2' is a value which approximates a physical analogue of oxygen, and is determined with a model developed by Izett and Tortell (2021) that is based on the historical physical forcing (wind, temperature, atmospheric pressure) in combination with measured N_2 to correct for biases. When using this model in calculating N_2' for this cruise, three-hour average directional components of wind speed and daily atmospheric pressure at mean sea level from NCEP North American Regional Reanalysis (NARR) provided by the NOAA/OAR/ESRL PSL, Boulder, Colorado, USA were used in calculating the historical wind speed and atmospheric pressure collocated with the cruise track for the 90 days prior to ship observations. (https://psl.noaa.gov/). Daily sea surface temperature (SST) based on NOAA High-resolution Blended Analysis of Daily SST and Ice data collocated with the cruise track provided by the NOAA/OAR/ESRL PSL, Boulder, Colorado, USA, from (https://psl.noaa.gov/) was used in modeling historical temperature. Salinity was assumed to remain constant, equal to the salinity measured at cruise sampling, while vertical mixing was ignored in these calculations due to lack of subsurface gas saturation data. The bubble scaling coefficient, β, was set to 0.5 for these calculations. This value was found to be optimal for the Izett and Tortell (2021) dataset, and sensitivity tests were conducted with this dataset that indicated our modeling results did not depend strongly on β.

Results and Discussion

Spatial patterns

A comparison of spatial distributions of ΔO_2 with $\Delta O_2/Ar$ for OS1901 illustrates how oxygen supersaturation and net biological oxygen supersaturation are related (Figure 1). Note that there are regions (e.g. red circle at 60°N) with strong oxygen supersaturation that are co-located with negative $\Delta O_2/Ar$, suggesting that oxygen supersaturation was purely driven by physical factors (e.g. wind and bubbles or warming). The biological signal was opposing this trend, but not completely compensating for physical effects. In other areas, ΔO_2 is greater than $\Delta O_2/Ar$,

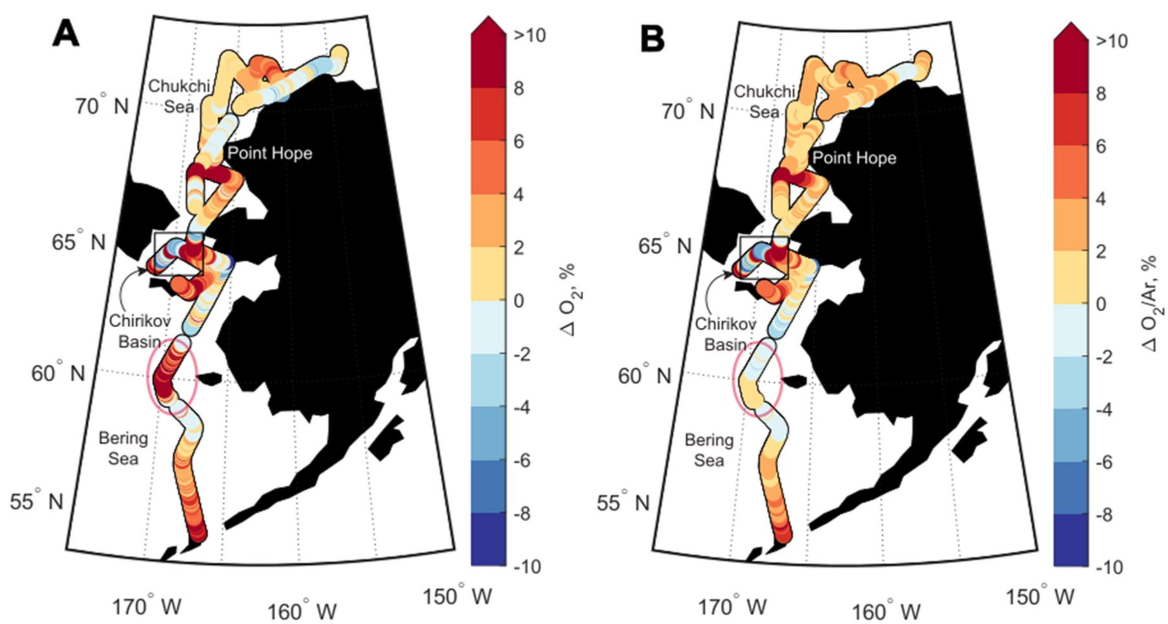

Figure 1: ΔO_2 and $\Delta O_2/Ar$ along the cruise track (scale attenuated to make near-equilibrium trends more visible). These trends in $\Delta O_2/Ar$ are also seen in $\Delta O_2/N_2$ (not shown here), while more noise is present in that signal. The cruise began in Dutch Harbor, AK and ended in Nome, AK. Breaks in the track line were due to gaps in data collection.

suggesting a mix of physical and biological forcing of oxygen supersaturation. The spatial patterns in $\Delta O_2/Ar$ indicate areas of large net biological supersaturation with $\Delta O_2/Ar$ peaks above 30% near the Aleutian arc, in Chirikov Basin and southwest of Point Hope. Regions in Chirikov Basin and southwest of Point Hope are established biological hotspots (Grebmeier et al. 2015).

In these biological hotspots, elevated underway chlorophyll-a (from a Seabird ECO-FL fluorometer) corresponded with high $\Delta O_2/Ar$ on 3 out of 4 instances (Figure 2). This anomalous result occurred in the region off of Point Hope which was occupied twice, on 8/11 and 8/23. While low concentrations of chlorophyll-a were observed during the first occupation, a chlorophyll peak was observed on the later occupation. A mismatch between chlorophyll-a and O_2/Ar is expected at times because of the different residence timescales associated with dissolved gases and chlorophyll production in the surface ocean: the O_2 signal from a bloom will take 2-3 weeks to reequilibrate with the atmosphere, whereas chlorophyll biomass can sink or be consumed by grazers over shorter timescales. Chlorophyll-a data from MODIS-Aqua (NASA Goddard Space Flight Group; Ocean Ecology Laboratory;

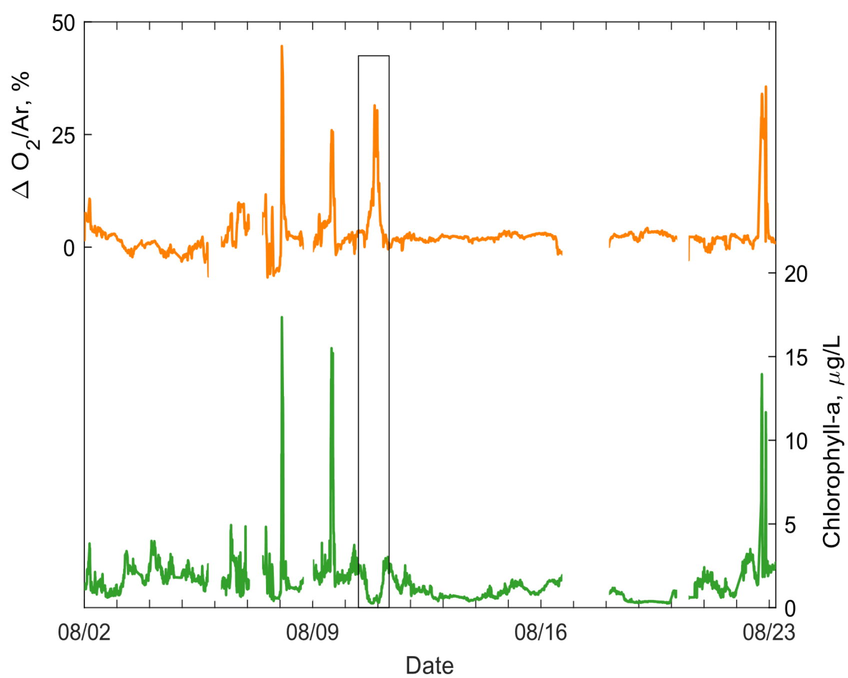

Figure 2: Underway measurements of $\Delta O_2/Ar$ and chlorophyll-a based on fluorescence throughout the cruise. Boxed area indicates occupation off of Pt. Hope with low chlorophyll and elevated $\Delta O_2/Ar$.

Ocean Biology Processing Group, https://modis.gsfc.nasa.gov/data/) were sparse in the weeks prior to shipboard measurements, but the edge of a bloom with elevated chlorophyll-a was seen off of Point Hope on August 4, 2019, about 7 days prior to shipboard measurements in the same location. This elevated biological production was indicated in the shipboard O_2/Ar, while the production of chlorophyll-a may have attenuated over a shorter timescale, resulting in low underway fluorescence.

In the Bering Sea, there are several regions where ΔO_2 is positive and ΔO_2/Ar is negative (Fig. 1), consistent with physical supersaturation of oxygen in the surface ocean due to both cooling water and increased wind speed (ΔO_2 >0) and net heterotrophic biological activity (ΔO_2/Ar <0). In Chirikov Basin, ΔO_2/Ar was variable, with patches of large supersaturation as well as undersaturation that could be attributed to the dynamic nature of water masses mixing in this area (Danielson et al. 2017). The areas with both negative and positive ΔO_2/Ar in the western part of Chirikov Basin are in significantly colder, saltier, nitrate-rich water (salinity >32.5, NO_3>20 μM from an underway nutrient sensor, data not shown) typical of Anadyr water (Grebmeier et al. 2006). The ΔO_2/Ar signals here likely reflect a combination of recent vertical mixing of subsurface water with a depleted O_2 signature to the surface and patchy production sparked by high nutrient Anadyr water when light and stratification conditions were favorable. In the majority of the Chukchi Sea, net biological oxygen supersaturation was positive, indicating net autotrophy (median ΔO_2/Ar=2% ±2.1%, median absolute deviation=0.8% when excluding biological hotspots where ΔO_2/Ar > 5%).

EIMS-GTD comparison

There was relative agreement between $\Delta O_2/N_2$ and ΔO_2/Ar for OS1901 with both ratios indicating net biological oxygen supersaturation for the majority of the cruise (Figure 3A). In areas of large biological oxygen supersaturation, the ratios are observed to differ, where $\Delta O_2/N_2$ is consistently larger than $\Delta O_2/Ar$ (Figure 3). The memory effects associated with the EIMS effectively slow down the $\Delta O_2/Ar$ measurements, resulting in $\Delta O_2/Ar$ that do not reach the true

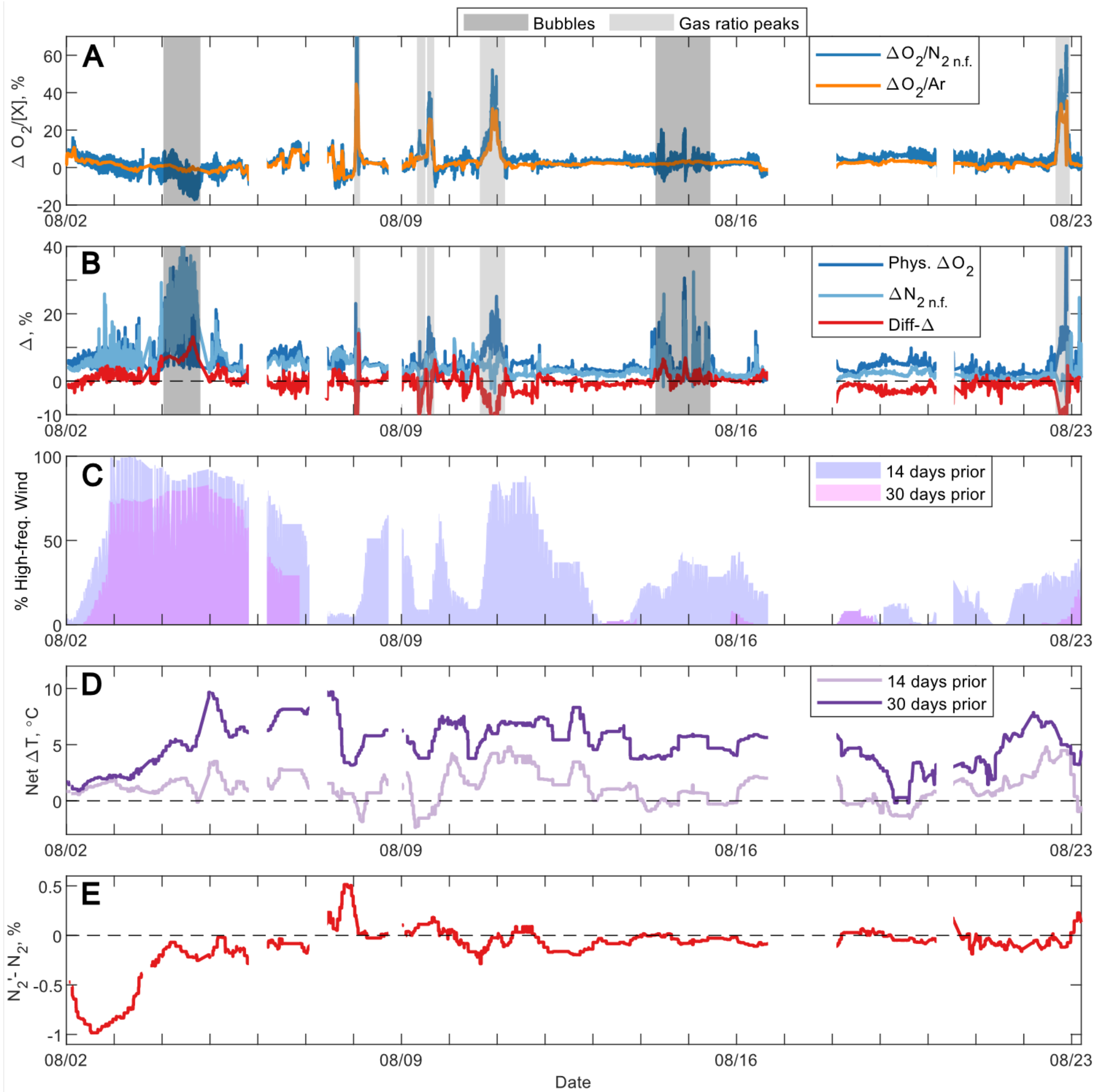

Figure 3: (A) Time-series of $\Delta O_2/Ar$ and noise-filtered (n.f.) $\Delta O_2/N_2$, where shaded areas indicate either noise due to bubbles in the underway seawater line or large gradients in gas ratios as determined by observation. The $\Delta O_2/N_2$ peak off the chart is at 127%. (B) Time-series of Diff-Δ, ΔO_2-physical, and noise-filtered ΔN_2, where artifacts of the data due to mismatched gas ratio peaks (Diff-Δ shaded in light gray) are off the chart and should not be considered. (C) Percent of 3-hourly average wind speed measurements exceeding 10 m s^{-1} over 14 and 30 days prior to sampling where collocated with cruise track. (D) Net temperature change over 14 and 30 days prior to sampling, collocated with cruise track, based on satellite SST reanalysis. (E) Difference between N_2' and N_2 along the cruise track.

maximum value during sharp gradients, while $\Delta O_2/N_2$ is thought to be capturing these maxima more accurately due to the faster response time. This difference in ratios in regions with large gradients is lessened by the exponentially filtered $\Delta O_2/N_2$ ratio, although this filter does not fully approximate the data smearing effects of the EIMS equilibrator. Large gradients may mask differences simply because of the mathematical differences of the filters applied to each method. This exponentially filtered data is only used when calculating diff-Δ, while noise-filtered $\Delta O_2/N_2$ is shown in all other plots.

By comparing $\Delta O_2/Ar$ and $\Delta O_2/N_2$ values with diff-Δ, biases of individual methods can be assessed. The median of diff-Δ over the cruise was -0.56%, indicating that $\Delta O_2/Ar$ was generally less than $\Delta O_2/N_2$, while there were many large excursions from these values (Figure 3B). In particular, deviations in diff-Δ occurred during time periods where strong gradients in oxygen were encountered and in areas with overwhelming bubble influence (shaded regions, Figure 3B). The spread of diff-Δ remains similar when observing all diff-Δ values compared to baseline values (which excludes erroneous data due to bubbles and steep gas peaks) (Figure 4), with a roughly normal distribution of diff-Δ where 90% of baseline observations fall between -3.6% and 2.6%.

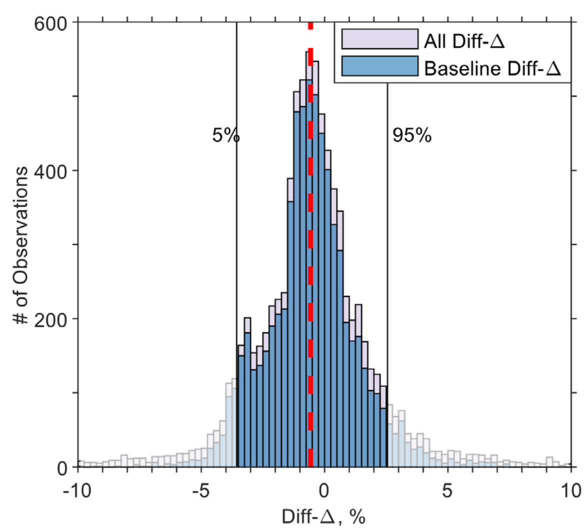

Figure 4: Histogram of diff-Δ observations with all values and with baseline values (when erroneous data due to bubbles and steep gas peaks are excluded).

A potential source of bias in $\Delta O_2/N_2$ and thus diff-Δ may arise from the assumed saturation of less prevalent gases, particularly Ar. On this cruise, Ar concentrations were determined by EIMS

O_2/Ar ratio and optode oxygen measurements (where $[Ar]=[O_2]_{optode}/[O_2/Ar]_{EIMS}$), yet these values were not used in calculations of $\Delta O_2/N_2$, as this study is intended to simulate the comparability of these methods, and the inclusion of calculated Ar values is not anticipated to be available with most GTD deployments. If these calculated values for Ar were included, which indicate Ar was consistently supersaturated throughout this cruise, the bias in diff-Δ does not change considerably, with a median of -0.50%.

Evaluating physically-driven bias in O_2/N_2 relative to O_2/Ar

Differences in ΔO_2/Ar and $\Delta O_2/N_2$, i.e., diff-Δ, are expected due to a variety of physical factors including gas solubility, bubble injection, and gas exclusion principles. For example, an increase in temperature instantaneously changes the gas solubility in the water mass; the solubility of Ar and O_2 will change similarly due to their comparable solubility, while N_2 solubility decreases to a lesser extent because it is less soluble. This difference in temperature effect between N_2 and Ar appears small in the individual gas saturation anomalies (Figure 5A) but becomes amplified when calculating gas ratios due to the dissimilarity between

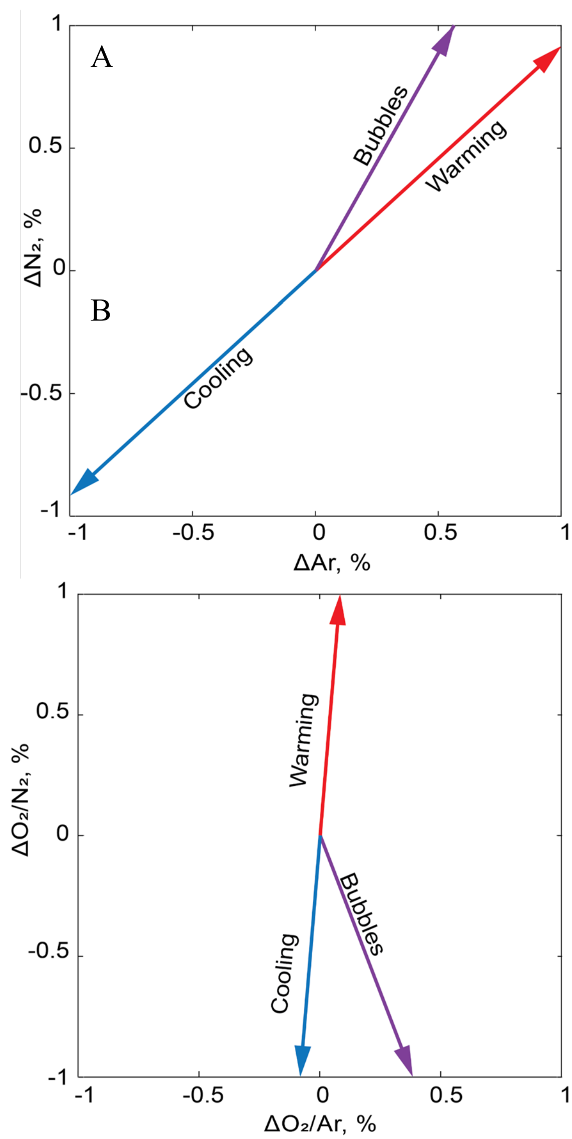

Figure 5: Expected changes in ΔAr, ΔN_2, ΔO_2/Ar and $\Delta O_2/N_2$ due to temperature change and bubble injection.

N_2 and O_2. The result is an $\Delta O_2/N_2$ ratio change in response to temperature that is 12 times greater than $\Delta O_2/Ar$ (Figure 5B). For example, warming of 5°C would result in relatively similar increases in O_2, N_2, and Ar saturations (11.3%, 10.4%, and 11.2% respectively) but pronounced differences between the $\Delta O_2/Ar$ and $\Delta O_2/N_2$ gas ratios (0.18% and 0.83% respectively). The resulting change in diff-Δ ($\Delta O_2/Ar$ - $\Delta O_2/N_2$) would be -0.65%. This warming-induced saturation signal will erode via exchange with the atmosphere over subsequent weeks as the upper ocean re-equilibrates to the new temperature (Figure 6A).

Conversely, wind-driven bubble injection creates a gas supersaturation due to enhanced gas injection which increases over the period of enhanced wind. Bubble injection and bubble exchange, parameterized as wind-driven based on the equations of Woolf and Thorpe (1991), will increase individual gas saturations but will decrease the $\Delta O_2/N_2$ ratio due to the high mole fraction of N_2 in the atmosphere and the relatively low solubility of N_2 in seawater. The wind-driven supersaturation of N_2 is much larger than the supersaturation of more soluble gases (O_2, Ar), such that enhanced wind will increase diff-Δ. If wind speed increases from 5 m/s to 15 m/s and remains at 15 m/s, the resulting

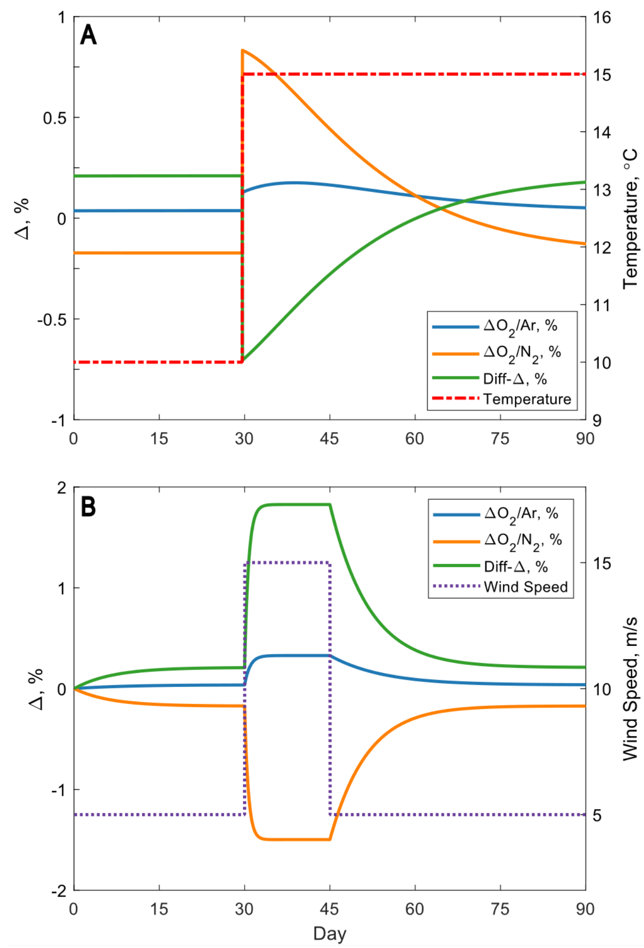

Figure 6: Box model of gas saturation change in $\Delta O_2/Ar$ and $\Delta O_2/N_2$ with (A) warming water and (B) increased wind speed. Baseline parameters include a mixed layer depth of 20 meters, temperature of 10°C, salinity of 32 and wind speed of 5 m/s.

equilibrium diff-Δ will reach a maximum of 1.8%, where diff-Δ will equal 95% of the maximum (1.8%) in 2 days based on the estimated effect of bubbles injected into the surface ocean and the solubility differences between N_2 and Ar (Fig 6B). The expected change in gas saturation and gas ratio saturation from temperature change and enhanced wind are indicated in Figure 6 where the relaxation back to equilibrium following either a high wind event or temperature change is slow (~ 6-8 weeks).

Because O_2/N_2 is likely to be more sensitive to physical forcing than O_2/Ar, one way of assessing causes of observed diff-Δ is by comparing diff-Δ values to an approximation of physical forcing, estimated as:

$$\Delta O_2^{phys} = \Delta O_2^{total} - \Delta O_2/Ar \quad (11)$$

where the last term (ΔO_2/Ar) represents ΔO_2^{bio} (Shadwick et al. 2015). When ΔO_2^{phys} is positive, a positive physical supersaturation of oxygen is estimated and could be indicative of recent warming of the water mass or potential influence of bubbles. Along the same lines, a negative value is expected when biological oxygen saturation is greater than total oxygen saturation, potentially caused by recent cooling. The estimate of ΔO_2^{phys} over this cruise has a mean value of 4.65% (Figure 3B).

We also calculated ΔN_2 as a tracer that is particularly sensitive to bubble-driven physical gas supersaturation. The mean ΔN_2 for the cruise was 4.2%. There appear to be similar patterns between average ΔO_2^{phys} and ΔN_2 (Figure 3B), yet the median negative diff-Δ (where negative diff-Δ results from warming and positive diff-Δ results from cooling and bubbles) suggests that warming is the primary driver of physical oxygen supersaturation, while the superimposed effects of bubbles or cooling could be also be contributing to the physical oxygen saturation estimated here.

The ΔO_2^{phys} estimated here is suggested to be due to recent warming of the water mass, based on the physical oxygen supersaturation and negative diff-Δ. The net temperature change over the preceding two weeks shows intermittent cooling and warming (Figure 3D), while the 30-day temperature change indicates warming throughout the cruise track (mean=5°C), a substantial warming that would have elevated oxygen supersaturation by a total of 11% over that period, contributing significantly to the overall positive ΔO_2^{phys}. This ΔO_2^{phys} is based on measurements from the time of the cruise, and any wind- and warming-driven components of ΔO_2^{phys} noted in the prior 30 days would have also been subject to reequilibration over that time period. A caveat in this analysis is that the net temperature change presented here is based on a fixed geo-referenced grid and does not consider water mass movement. For example, if a recently warmed water parcel horizontally advected into an area on the cruise track, the net temperature change calculated based on satellite SST for a fixed location will not record the true temperature history of the sampling location.

Despite the evidence suggesting warming is the primary driver of ΔO_2^{phys}, there is also a strong correlation between ΔO_2^{phys} and ΔN_2, where ΔN_2 is susceptible to both bubble-influence and temperature change. To achieve a solely bubble-driven N_2 supersaturation of 4%, similar to the estimated average for this cruise, wind speed would need to be greater than 15 m s^{-1} for a short period of time. We looked at daily wind speeds, which were likely not sufficient in capturing short-lived wind events that play a large role in bubble processes. This resulted in using 3-hour wind speeds, which are expected to better represent what is relevant from a bubble perspective due to the quick response of dissolved gas saturation to an increase in wind speed (Figure 6B), yet these did not support the hypothesis of wind-driven bubbles contributing strongly to the observed ΔN_2. Three-hourly wind speeds from NCEP NARR Reanalysis were used to calculate maximum wind speed and the percent of high-frequency winds (Figure 3C), as determined by the number of observations with wind speed >10 m s^{-1} in the preceding 14 and 30 days. These historical estimates of wind forcing are not correlated to overall diff-Δ signals on this cruise, aside from excluded regions known to be bubble-dominated, and this is likely due to the cumulative effects from wind and temperature change, as well as other factors not estimated here (vertical mixing, salinity, atmospheric pressure). While physical forcing estimates were not directly related to observed diff-Δ over the span of this cruise, a more accurate approach of modeling water mass history could better approximate the solubility-based differences between O_2/Ar and O_2/N_2.

Recently, Izett and Tortell (2020b) introduced a calculated value, N_2', that corrects for solubility differences between N_2 and Ar using historical water mass data, where N_2' is an approximation of Ar, a physical analog to O_2 (Izett and Tortell 2020b; Izett et al. 2021). If N_2' and N_2 differ significantly, a large component of physical bias was corrected for, suggesting O_2/N_2 may not be a good tracer of net biological oxygen production, while small differences indicate that O_2/N_2 may be a useful approximation of net biological oxygen production due to the similarity in physical solubility differences between N_2 and O_2 for a particular dataset. Our estimated N_2' is similar to measured N_2 for most of this cruise (Figure 3E), with deviations that may be attributed to wind and temperature change (Figure 8).

Over the first two days of the cruise in the southern Bering Sea, wind was the predominant driver of the negative difference between N_2' and N_2, which was also the case intermittently over the following two days (Figure 8B). This was determined based on both the relatively high-frequency winds, small temperature change (Figure 3), and the results of a pair of N_2' modeling calculations in which either historical temperature or wind was held constant at values measured on the cruise (Figure 8). After the initial wind-dominated days in the Bering Sea, the combination of wind and warming temperatures resulted in near-zero difference in N_2' and N_2, where the two factors likely balanced each other out at times.

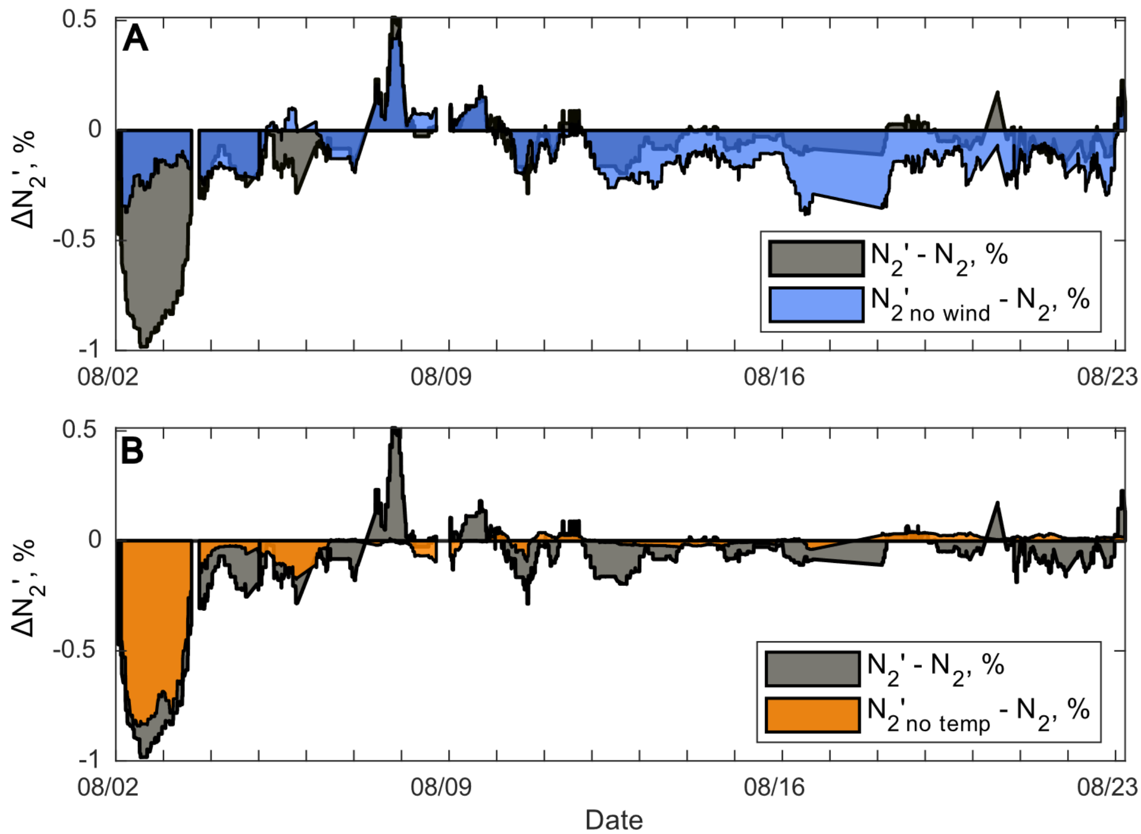

Figure 7: (A) Modeled $N_2' - N_2$ compared to $N_2'_{no\ wind} - N_2$, modeled when historical wind speed is set constant, equal to wind speed at cruise occupation. Areas where these align indicate that historical wind speed is not the main driver of saturation differences, and suggests that temperature is the main driver. (B) Modeled $N_2' - N_2$ compared to $N_2'_{no\ temp} - N_2$ when historical sea surface temperature is set constant, equal to temperature at cruise occupation. Areas where these are similar indicate that historical temperature change is not the main driver of saturation differences, and suggests that wind is the main driver.

The difference in N_2' and N_2 throughout the cruise was not directly correlated to the estimates of physical forcing described here (high-frequency wind, average wind speed, and net temperature change over 14 and 30 days). This is suspected to be in part due to the cumulative nature of physical forcing, inaccuracies in satellite-based wind speeds, and the averaging that was used in these estimates, where wind and temperature changes in the day or two prior to measurement will be more strongly reflected in N_2' than those two weeks prior. Additionally, the calculations of N_2' performed here excluded vertical mixing due to lack of gas saturation data at depth, yet absence of vertical mixing is unlikely and therefore contributes to error in estimated N_2'. The small differences in N_2' and N_2 throughout most of this cruise are consistent with findings by Izett et al. (2021) in the Canadian Arctic Archipelago and Baffin Bay over the period of observations, which were also minimal. The use O_2/N_2' could improve the utility of the GTD method in many regions, yet the advective nature of water masses should be accounted for in a study area, where highly advective regions may be inaccurately modeled by georeferenced data prior to sampling. In this study, the difference between N_2 (used in calculating diff-Δ) and N_2' could result in errors in the calculated diff-Δ at times, assuming N_2' is more accurate than N_2.

Sea ice and biological influences on dissolved O_2, N_2, and Ar

Other factors that influence gas saturation include sea ice formation, sea ice melt, and biologically-driven N_2 fixation or denitrification. For this dataset, we expect these processes to contribute insignificantly toward driving differences between O_2/N_2 and O_2/Ar. During sea ice formation, brine rejected from the ice matrix is expected to be enriched in Ar, O_2, and N_2 due to the exclusion of larger gas molecules during the freezing process. This brine sinks to depth, enriching deep water in these gases. When vertical mixing of these deep waters occurs, a brine signal may be observed in the resulting water, which is expected to be enriched in Ar compared to N_2 based on gas partitioning between bubbles, ice, brine, and residual water (Hood 1998; Hood et al. 1998). In contrast, the meltwater signal is expected to be depleted in larger gases (Ar, O_2, N_2) due to gas exclusion during sea ice formation. This meltwater effect is not anticipated to be represented in this dataset due to lack of sea ice during and directly prior to this cruise, but brine signatures could be observed in areas where vertical mixing brings waters that have been seasonally isolated at depth to the surface.

Biological influences on dissolved N_2 in the ocean, including nitrogen fixation and denitrification, typically have a small overall effect on dissolved N_2 saturation (ΔN_2). The effect of nitrogen fixation, calculated based on the maximum rate of nitrogen fixation estimated by Shiozaki (2018) in the Chukchi Sea, is negligible on ΔN_2 (<0.01%). The effect of denitrification on the shallow Bering and Chukchi shelves has a potentially greater effect on N_2. Vertical mixing of deep water containing biologically elevated dissolved N_2 will influence the O_2/N_2 ratios measured at the surface, resulting in lower than expected $\Delta O_2/N_2$. With seasonal dissolved inorganic nutrient deficits (3.9 μM N) at depth on the Chukchi shelf (Mordy et al. 2021), vertical mixing of 20% of the water column would result in a 0.06% decrease in $\Delta O_2/N_2$ in the surface mixed layer, a small and likely indiscernible bias. Since the Chukchi Sea is seasonally well-stratified, more significant vertical mixing of the water column is only likely to occur near coastal features or areas with enhanced mixing, such as near Bering Strait.

Net Community Production

The median NCP estimated by O_2/Ar and O_2/N_2 was 7.33 ± 2.43 and 9.43 ± 2.73 mmol O_2 m^{-2} day^{-1}, respectively, for all regions with comparable data (which excludes bubble-impacted areas, as well as one region in Chirikov Basin with a clear vertical mixing signal). The overall NCP estimated by O_2/Ar and O_2/N_2 are similar, while differences include the discrepancy in maximum NCP in regions with large gradients as previously discussed, as well as increased noise in O_2/N_2 signal (Figure 9).

The median NCP based on O_2/Ar measurements was 7.6 mmol O_2 m^{-2} day^{-1}, while 95% of the values fell between -15.9 and 59.8 mmol O_2 m^{-2} day^{-1}. Assuming NCP is primarily new production fueled by nitrate, we use an O_2:C ratio of 1.4 (Laws 1991), where O_2/Ar-based NCP ranged from below zero to >1000 mg C m^{-2} day^{-1}, with a median of 67 mg C m^{-2} day^{-1} during this August cruise. Since this measurement technique integrates over the preceding weeks, this unique dataset may better capture episodic events that are missed by shorter-term incubations. These measurements therefore fill an important temporal gap between short-term incubations and large-scale seasonal drawdown estimates calculated at the regional scale.

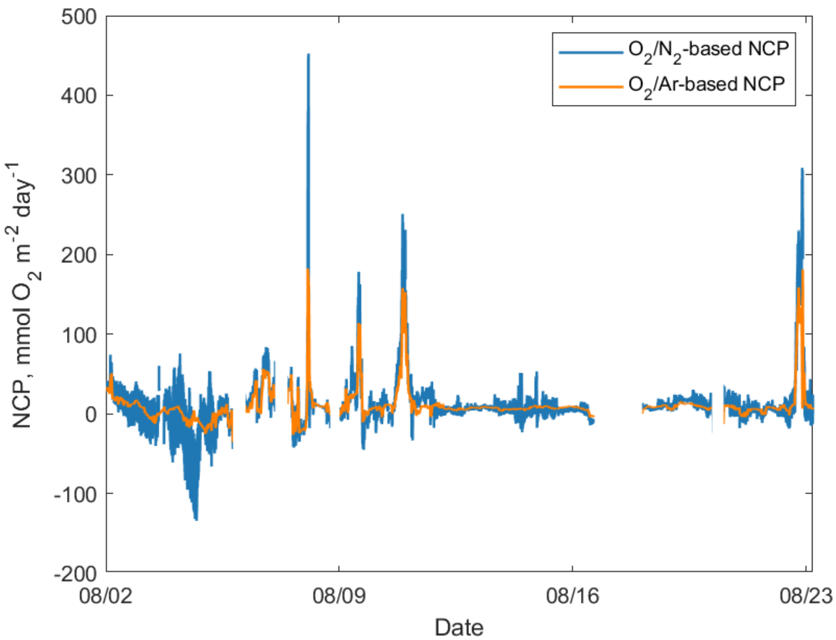

Figure 8: NCP calculated based on O_2/Ar and residual filtered O_2/N_2 for measurements within the bounds described.

Seasonal estimates based on DIC and nutrient drawdown (Mathis et al. 2009; Codispoti et al. 2013) include the spring bloom, and are therefore expected to be considerably higher than the rates measured in August, post-bloom, while annual measurements (Mordy et al. 2020) include the dark, ice-covered winter when production is absent. The NCP values from this dataset are generally in line with others in the Chukchi Sea which do not include the spring bloom production (Table 1).

With the spatially resolved data from this cruise, local hotspots can be assessed, and potential drivers of biological production can also be explored. Areas of high net biological productivity from this cruise were consistent with previously observed biological hotspots in the Chirikov Basin and off of Point Hope (Distributed Biological Observatory regions 2 and 3, respectively, Grebmeier et al. 2010). This data supports the suggestion that production is patchy (Juranek et al. 2019), patterns that may be missed by traditional incubation sampling approaches. Patchy regions of high NCP on this cruise may be a result of nutrient input through the convergence of water masses, which was noted in Chirikov Basin where Anadyr water was present, as well as near Pt. Hope due to the combination of upstream mixing in Bering Strait and water flow around the headland of Pt. Hope (Figure 10). In the Pt. Hope region, the high NCP observed by gas ratio methods, which at times contrasted with the measured chlorophyll, was indicative of the

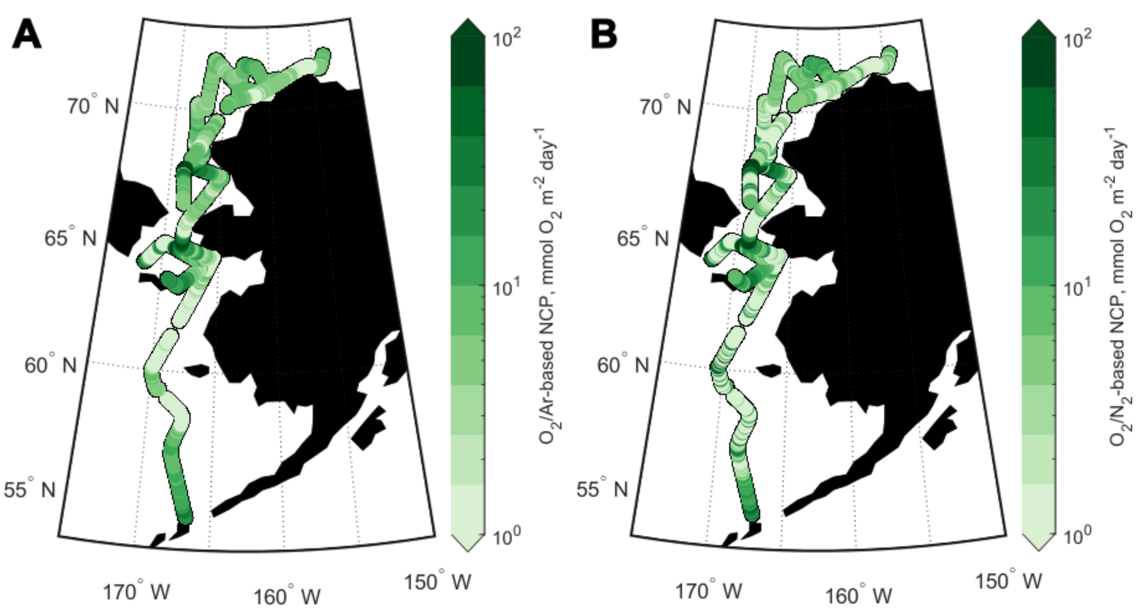

Figure 9 : O_2/Ar-based NCP and O_2/N_2-based NCP along the cruise track (scale attenuated, where range is -35 to 182 and -144 to 528, respectively).

intermittent nature of blooms in this region. These variations are due to the coexistence of favorable light and nutrient conditions, which can vary due to changes in water masses, mixed layer depth, and/or wind patterns. Better understanding of marine productivity patterns and how they relate to water mass convergences and wind events could help to decipher the dynamic environmental factors driving this production.

Uncertainty analysis

To estimate uncertainty in EIMS- and GTD-based NCP, we used a Monte Carlo approach that involves randomly varying the estimated error of each parameter involved in calculating NCP, assuming a normal distribution of error. The values used in these determinations are found in Table 1, where uncertainty was calculated based on 1000 determinations of $\Delta O_2/Ar$- and $\Delta O_2/N_2$-based NCP with Equation 10 for gas ratios observed on this cruise. Absolute uncertainty in the measurement of O_2/Ar of ± 0.25% was determined by the standard deviation of O_2/Ar in air standards (n=27) measured by IRMS, since EIMS O_2/Ar measurements were corrected to the calibration bottle samples analyzed by IRMS. For GTD-based measurements, an absolute

Table 1: NCP comparisons in Chukchi Sea

Method	**NCP (mg C m^{-2} day^{-1})**	**Region**	**Timescale**	**Source**
DIC Drawdown	8 to >2000 (range of values)	Northeast Chukchi Sea	Seasonal, spring to summer	Mathis et al. 2009
Nutrient drawdown	1167	Southern Chukchi Sea	60-day growing period	Codispoti et al. 2013
Seasonal nitrate	82 to 192	Eastern Chukchi Sea	Annual, between 2010-2018	Mordy et al. 2020
Shipboard O_2/Ar	8 to 86 [1 to 10 mmol O_2 m^{-2} day^{-1}]	Chukchi Sea	Integrated over few weeks in October 2011 and 2012	Juranek et al. 2019
Shipboard O_2/Ar	67 [7.6 mmol O_2 m^{-2} day^{-1}]	Chukchi Sea	Integrated over few weeks in August 2019	this study

precision in the measurement and calculation of O_2/N_2 of ±0.57% was determined by propagation of error in Equations 6 and 7 (Table 2).

Uncertainty in the gas transfer coefficient, k_{O2} (± 20%) (Wanninkhof 2014), makes up the largest component of uncertainty in NCP. The resulting uncertainty for a simulated NCP of 10 mmol O_2 per m^2-day from O_2/Ar and O_2/N_2 is 22% and 35%, respectively, with a proportionally lower error with larger NCP rate. The uncertainty in O_2/Ar-based NCP ranged from 16% to >100%, while the uncertainty for O_2/N_2-based NCP ranged from 21% to >100%. Importantly, while uncertainty in $\Delta O_2/N_2$ becomes large in areas where net biological oxygen supersaturation nears zero, these estimates still discern the relative magnitude and direction of NCP for the majority of observations on this cruise, so long as the oxygen measurements used to compute O_2/N_2 are well-calibrated.

The uncertainty outlined above is based on the accuracy in the measurement and calculation of $\Delta O_2/N_2$, and does not include potential biases from physical forcing that cause this tracer to inaccurately track ΔO_{2bio} (see ‘Evaluating

Table 2: Error estimates used in Monte Carlo approach of uncertainty and output uncertainty in $\Delta O_2/Ar$ and $\Delta O_2/N_2$.

Source	**Estimated Error**
O_2/Ar_{meas}	0.25% (St. Dev. Of O_2/Ar in air)
O_{2sol}	0.3% (Garcia and Gordon 1992)
Gas exchange, k	20% (Wanninkhof 2014)
GTD total pressure	0.2% or 2 mbar (Pro-Oceanus TDGP manual)
O_2 (Winkler-corrected optode)	0.5% or 1.1 mbar (McNeil et al. 2005)
Atmospheric pressure (NCEP reanalysis)	0.5% or 5 mbar (Padin et al. 2007)

Uncertainty			
	Absolute	Relative	
		$\Delta O_2/[X]$ = 1%	$\Delta O_2/[X]$ = 10%
O_2/Ar	0.25%	40.2%	4.1%
O_2/N_2	0.57%	67.7%	7.6%

physically-driven bias in O_2/N_2 relative to O_2/Ar'). When comparing diff-Δ to the methodological uncertainty of 0.57% in $\Delta O_2/N_2$, the bias represented by diff-Δ has a relatively small effect. The distribution of baseline diff-Δ -3.6% and 2.6% for 90% of observations is attributed to the cumulative saturation effects of both bubbles and temperature change, while potential variations in Ar saturation could have also played a role. Bubbles were the primary driver in the southern Bering Sea, while temperature change became more important in the Chukchi Sea, as inferred from the modeling described above.

Strengths and weaknesses of GTD and EIMS approaches

A potential limitation of gas ratio estimates from a GTD is the dependence on accurate oxygen measurements when calculating O_2/N_2. This requires optode calibration to adjust for offsets and drift, where a 5% offset in the optode O_2 (the average offset on this cruise), results in a difference of 6.5% in O_2/N_2. Without reliable oxygen calibrations, this scale of difference could result in ambiguous NCP estimates derived from O_2/N_2, although areas with strong biological signals are still qualitatively identified despite this potential uncertainty. This is expected to be a greater issue when frequent O_2 calibration samples are not feasible, e.g. with autonomous deployments, although periodic air calibration of deployed optodes could serve as an alternative calibration method (Bittig and Körtzinger 2015; Bushinsky et al. 2016).

Another challenge experienced with the GTD-optode system on this cruise was the effect of bubbles. Bubble effects are likely to be a problem for ships with shallow seawater intakes (<5 m) operating in moderate to rough sea states. While a debubbling chamber could be employed to limit this noise, areas with extensive bubble influence in the GTD/optode data are expected to be influenced by bubble injection and exchange in the water column as well, which would still bias the measured O_2/N_2.

This methods comparison revealed a smoothing of oxygen peaks in the EIMS data, which we attribute to the EIMS equilibrator memory effect. Optode O_2 and GTD-based O_2/N_2 peaks were much sharper and reached higher maximum values in biological hotspots; in these areas, the observed $\Delta O_2/N_2$ was up to 1.5 times greater than $\Delta O_2/Ar$. Therefore, in regions with sharp gradients and localized productivity peaks, such as those encountered in this study in the Chirikov basin and the vicinity of Pt. Hope, GTD measurements may more accurately capture absolute productivity values, while EIMS-based observations are likely a better choice in oligotrophic, lower-productivity regions that characterized the rest of the cruise track. On future deployments, EIMS equilibrator response times could also be better optimized by using an equilibrator cartridge with a smaller headspace to water volume ratio, while including a recirculating desiccant loop for constant removal of water vapor in the equilibrator has also been shown to improve response time (Manning et al. 2016).

Conclusions

This cruise provided a range of conditions under which to assess the efficacy of the GTD/optode system compared to the EIMS for estimating net biological oxygen production. An important takeaway from this method comparison is the relatively quick response time of the GTD, which allows sharp gradients in gas saturation to be well characterized. This method is subject to greater biases from temperature change and bubble injection than the more commonly used O_2/Ar approach. However, by using historical modeling to approximate O_2/N_2' (Izett and Tortell 2021) or by utilizing time series measurements on a mooring or drifter that could record the physical changes over time in a given water mass, the expected divergence of $\Delta O_2/N_2$ from $\Delta O_2/Ar$ can be estimated.

The utility of this method depends on the productivity in an area: the GTD/optode system is expected to capture large signals in net biological oxygen supersaturation, while oligotrophic areas with low net productivity may be more difficult to determine with certainty. If physical factors influencing solubility are decomposed and accounted for, as Izett and Tortell (2021) do with O_2/N_2', the near-equilibrium $\Delta O_2/N_2$ can still be used as an estimate of biological oxygen, with some inherent uncertainty. In this study, $\Delta O_2/N_2$ was typically greater than $\Delta O_2/Ar$, overestimating net biological production throughout most of the cruise. In regions with very low production, the use of $\Delta O_2/N_2$ could result in a productivity estimate of the opposite sign as from $\Delta O_2/Ar$, yet the use of $\Delta O_2/N_2$' (Izett and Tortell 2021) provides a promising method to narrow the difference between tracers using water mass history.

The dependence of $\Delta O_2/N_2$ on calibrated oxygen measurements also needs to be considered when using the GTD/optode method in an autonomous deployment. By incorporating periodic air measurements by the optode, a strategy that has previously been used on floats (Bittig and Körtzinger 2015), reliable oxygen measurements could be maintained throughout a GTD/optode deployment, providing a reference for calibration.

NCP over the course of this cruise was patchy, with localized areas of high NCP associated with known biological hotspots. The NCP derived from both $\Delta O_2/Ar$ and $\Delta O_2/N_2$ captured this patchiness because dissolved gases in the surface ocean integrate processes over a longer time history (2-3 weeks) than the shorter-term measurements reflected by bottle incubations or chlorophyll concentrations. This GTD/optode method provides spatially and temporally high-resolution NCP observations, with potential for autonomous observations in the future. This data allows for improved understanding of net community production and the mechanisms driving this production in dynamic coastal regions.

Acknowledgements

We thank Sarah Donohoe for her analysis of oxygen samples at sea. We also thank the captain and crew of R/V *Ocean Starr* for their shipboard support. This cruise was part of the Arctic Integrated Ecosystem Survey (Arctic IES), funded as part of the North Pacific Research Board's (NPRB's) Arctic Integrated Ecosystem Research Program (IERP). This work was supported by NSF awards 1928684 and 1949593 and Simons Foundation 329104 to LWJ. This project is part of the Innovative Technology for Arctic Exploration (ITAE) program funded by NOAA's Pacific Marine Environmental Laboratory (NOAA/PMEL). This publication is partially funded by the Joint Institute for the Study of the Atmosphere and Ocean under NOAA Cooperative Agreement NA15OAR4320063. This is contribution No. 5264 for the Pacific Marine Environmental Laboratory, contribution No. 1146 for CICOES, and contribution No. 1011 for NOAA's Ecosystem Fisheries Oceanography Coordinated Investigations.

References

Andersen, J. K., L. M. Andreassen, E. H. Baker, and others. 2020. State of the Climate in 2019: The Arctic J. Richter-Menge and M.L. Druckenmiller [eds.]. Bull. Am. Meteorol. Soc. **101**: S239–S286. doi:10.1175/BAMS-D-20-0086.1

Anderson, L. G., and S. Kaltin. 2001. Carbon fluxes in the Arctic Ocean—potential impact by climate change. Polar Res. **20**: 225–232. doi:10.3402/polar.v20i2.6521

Arrigo, K. R., and G. L. van Dijken. 2015. Continued increases in Arctic Ocean primary production. Prog. Oceanogr. **136**: 60–70. doi:10.1016/j.pocean.2015.05.002

Arrigo, K. R., G. van Dijken, and S. Pabi. 2008. Impact of a shrinking Arctic ice cover on marine primary production. Geophys. Res. Lett. **35**: 1–6. doi:10.1029/2008GL035028

Bélanger, S., M. Babin, and J.-É. Tremblay. 2013. Increasing cloudiness in Arctic damps the increase in phytoplankton primary production due to sea ice receding. Biogeosciences **10**: 4087–4101. doi:10.5194/bg-10-4087-2013

Benson, B. B., and D. Krause. 1984. The concentration and isotopic fractionation of oxygen dissolved in freshwater and seawater in equilibrium with the atmosphere1. Limnol. Oceanogr. **29**: 620–632. doi:10.4319/lo.1984.29.3.0620

Bittig, H. C., and A. Körtzinger. 2015. Tackling oxygen optode drift: Near-surface and in-air oxygen optode measurements on a float provide an accurate in situ reference. J. Atmos. Ocean. Technol. **32**: 1536–1543. doi:10.1175/JTECH-D-14-00162.1

Bushinsky, S. M., S. R. Emerson, S. C. Riser, and D. D. Swift. 2016. Accurate oxygen measurements on modified argo floats using in situ air calibrations. Limnol. Oceanogr. Methods **14**: 491–505. doi:10.1002/lom3.10107

Carmack, E. C., and P. Wassmann. 2006. Food webs and physical–biological coupling on pan-Arctic shelves: Unifying concepts and comprehensive perspectives. Prog. Oceanogr. **71**: 446–477. doi:10.1016/j.pocean.2006.10.004

Carmack, E., I. Polyakov, L. Padman, and others. 2015. Toward quantifying the increasing role of oceanic heat in sea ice loss in the new arctic. Bull. Am. Meteorol. Soc. **96**: 2079–2105. doi:10.1175/BAMS-D-13-00177.1

Carpenter, J. H. 1965. The Accuracy of the Winkler Method for Dissolved Oxygen Analysis. Limnol. Oceanogr. **10**: 135–140. doi:10.4319/lo.1965.10.1.0135

Cassar, N., B. A. Barnett, M. L. Bender, J. Kaiser, R. C. Hamme, and B. Tilbrook. 2009. Continuous High-Frequency Dissolved O_2/Ar Measurements by Equilibrator Inlet Mass

Spectrometry. Anal. Chem. **81**: 1855–1864. doi:10.1021/ac802300u

Codispoti, L. A., V. Kelly, A. Thessen, P. Matrai, S. Suttles, V. Hill, M. Steele, and B. Light. 2013. Synthesis of primary production in the Arctic Ocean: III. Nitrate and phosphate based estimates of net community production. Prog. Oceanogr. **110**: 126–150. doi:10.1016/j.pocean.2012.11.006

Craig, H., and T. Hayward. 1987. Oxygen Supersaturation in the Ocean: Biological Versus Physical Contributions. Science (80-.). **235**: 199–202. doi:10.1126/science.235.4785.199

Danielson, S. L., O. Ahkinga, C. Ashjian, and others. 2020. Manifestation and consequences of warming and altered heat fluxes over the Bering and Chukchi Sea continental shelves. Deep. Res. Part II Top. Stud. Oceanogr. **177**. doi:10.1016/j.dsr2.2020.104781

Danielson, S. L., L. Eisner, C. Ladd, C. W. Mordy, L. Sousa, and T. J. Weingartner. 2017. A comparison between late summer 2012 and 2013 water masses, macronutrients, and phytoplankton standing crops in the northern Bering and Chukchi Seas. Deep. Res. Part II Top. Stud. Oceanogr. **135**: 7–26. doi:10.1016/j.dsr2.2016.05.024

DeGrandpre, M., W. Evans, M. L. Timmermans, R. Krishfield, B. Williams, and M. Steele. 2020. Changes in the Arctic Ocean Carbon Cycle With Diminishing Ice Cover. Geophys. Res. Lett. **47**. doi:10.1029/2020GL088051

Ducklow, H., and S. C. Doney. 2013. What is the metabolic state of the oligotrophic ocean? a debate. Ann. Rev. Mar. Sci. **5**: 525–533. doi:10.1146/annurev-marine-121211-172331

Emerson, S. R., C. Stump, B. Johnson, and D. M. Karl. 2002. In situ determination of oxygen and nitrogen dynamics in the upper ocean. Deep Sea Res. Part I Oceanogr. Res. Pap. **49**: 941–952. doi:10.1016/S0967-0637(02)00004-3

Emerson, S. R., C. Stump, and D. Nicholson. 2008. Net biological oxygen production in the ocean: Remote in situ measurements of O 2 and N 2 in surface waters. Global Biogeochem. Cycles **22**: n/a-n/a. doi:10.1029/2007GB003095

Emerson, S. R., B. Yang, M. White, and M. Cronin. 2019. Air-Sea Gas Transfer: Determining Bubble Fluxes With In Situ N2 Observations. J. Geophys. Res. Ocean. **124**: 2716–2727. doi:10.1029/2018JC014786

Eveleth, R., N. Cassar, R. M. Sherrell, H. Ducklow, M. P. Meredith, H. J. Venables, Y. Lin, and Z. Li. 2017. Ice melt influence on summertime net community production along the Western Antarctic Peninsula. Deep. Res. Part II Top. Stud. Oceanogr. **139**: 89–102. doi:10.1016/j.dsr2.2016.07.016

Eveleth, R., M. L. Timmermans, and N. Cassar. 2014. Physical and biological controls on oxygen saturation variability in the upper Arctic Ocean. J. Geophys. Res. Ocean. **119**: 7420–7432. doi:10.1002/2014JC009816

Garcia, H. E., and L. I. Gordon. 1992. Oxygen solubility in seawater: Better fitting equations. Limnol. Oceanogr. **37**: 1307–1312. doi:10.4319/lo.1992.37.6.1307

Glueckauf, E. 1951. The Composition of Atmospheric Air, p. 3–10. *In* Compendium of Meteorology. American Meteorological Society.

Grebmeier, J. M., B. A. Bluhm, L. W. Cooper, and others. 2015. Ecosystem characteristics and processes facilitating persistent macrobenthic biomass hotspots and associated benthivory in the Pacific Arctic. Prog. Oceanogr. **136**: 92–114. doi:10.1016/j.pocean.2015.05.006

Grebmeier, J. M., L. W. Cooper, H. M. Feder, and B. I. Sirenko. 2006. Ecosystem dynamics of the Pacific-influenced Northern Bering and Chukchi Seas in the Amerasian Arctic. Prog.

Oceanogr. **71**: 331–361. doi:10.1016/j.pocean.2006.10.001

Grebmeier, J. M., S. E. Moore, J. E. Overland, K. E. Frey, and R. Gradinger. 2010. Biological Response to Recent Pacific Arctic Sea Ice Retreats. Eos, Trans. Am. Geophys. Union **91**: 161. doi:10.1029/2010EO180001

Hamme, R. C., N. Cassar, V. P. Lance, and others. 2012. Dissolved O2/Ar and other methods reveal rapid changes in productivity during a Lagrangian experiment in the Southern Ocean. J. Geophys. Res. Ocean. **117**: 1–19. doi:10.1029/2011JC007046

Hamme, R. C., and S. R. Emerson. 2004. The solubility of neon, nitrogen and argon in distilled water and seawater. Deep. Res. Part I Oceanogr. Res. Pap. **51**: 1517–1528. doi:10.1016/j.dsr.2004.06.009

Hamme, R. C., and S. R. Emerson. 2006. Constraining bubble dynamics and mixing with dissolved gases: Implications for productivity measurements by oxygen mass balance. J. Mar. Res. **64**: 73–95. doi:10.1357/002224006776412322

Harada, N. 2016. Review: Potential catastrophic reduction of sea ice in the western Arctic Ocean: Its impact on biogeochemical cycles and marine ecosystems. Glob. Planet. Change **136**: 1–17. doi:10.1016/j.gloplacha.2015.11.005

Hendricks, M. B., M. L. Bender, and B. A. Barnett. 2004. Net and gross O2 production in the southern ocean from measurements of biological O2 saturation and its triple isotope composition. Deep. Res. Part I Oceanogr. Res. Pap. **51**: 1541–1561. doi:10.1016/j.dsr.2004.06.006

Hill, V. J., and G. Cota. 2005. Spatial patterns of primary production on the shelf, slope and basin of the Western Arctic in 2002. Deep Sea Res. Part II Top. Stud. Oceanogr. **52**: 3344–

3354. doi:10.1016/j.dsr2.2005.10.001

Hood, E. 1998. Hood (1998).pdf.

Hood, E. M., B. L. Howes, and W. J. Jenkins. 1998. Dissolved gas dynamics in perennially ice-covered Lake Fryxell, Antarctica. Limnol. Oceanogr. **43**: 265–272. doi:10.4319/lo.1998.43.2.0265

Izett, R., and P. Tortell. 2020. The Pressure of In Situ Gases Instrument (PIGI) for Autonomous Shipboard Measurement of Dissolved O2 and N2 in Surface Ocean Waters. Oceanography **33**. doi:10.5670/oceanog.2020.214

Izett, R. W. 2021. O2N2 NCP Toolbox (version 2021.05).doi:https://doi.org/10.5281/zenodo.4024925

Izett, R. W., R. C. Hamme, C. L. McNeil, C. C. Manning, A. Bourbonnais, and P. Tortell. 2021. ΔO2/N2' as a new tracer of marine net community production: Application and evaluation in the Subarctic Northeast Pacific and Canadian Arctic Ocean. Front. Mar. Sci.

Izett, R. W., and P. D. Tortell. 2021. <scp> ΔO $_2$ </scp> / <scp> N $_2$ </scp> ′ as a tracer of mixed layer net community production: Theoretical considerations and proof-of-concept. Limnol. Oceanogr. Methods **19**: 497–509. doi:10.1002/lom3.10440

Juranek, L. W., and P. D. Quay. 2005. In vitro and in situ gross primary and net community production in the North Pacific Subtropical Gyre using labeled and natural abundance isotopes of dissolved O 2. Global Biogeochem. Cycles **19**: 1–15. doi:10.1029/2004GB002384

Juranek, L. W., P. D. Quay, R. A. Feely, D. Lockwood, D. M. Karl, and M. J. Church. 2012. Biological production in the NE Pacific and its influence on air-sea CO 2 flux: Evidence from dissolved oxygen isotopes and O_2/Ar. J. Geophys. Res. Ocean. **117**. doi:10.1029/2011JC007450

Juranek, L. W., T. Takahashi, J. T. Mathis, and R. S. Pickart. 2019. Significant Biologically Mediated CO_2 Uptake in the Pacific Arctic During the Late Open Water Season. J. Geophys. Res. Ocean. **124**: 1–23. doi:10.1029/2018JC014568

Kaiser, J., M. K. Reuer, B. A. Barnett, and M. L. Bender. 2005. Marine productivity estimates from continuous O_2/Ar ratio measurements by membrane inlet mass spectrometry. Geophys. Res. Lett. **32**. doi:10.1029/2005GL023459

Laws, E. A. 1991. Photosynthetic quotients, new production and net community production in the open ocean. Deep Sea Res. Part A. Oceanogr. Res. Pap. **38**: 143–167. doi:10.1016/0198-0149(91)90059-O

Lewis, K. M., G. L. Van Dijken, and K. R. Arrigo. 2020. Changes in phytoplankton concentration now drive increased Arctic Ocean primary production. Science (80-.). **369**: 198–202. doi:10.1126/science.aay8380

Lockwood, D., P. D. Quay, M. T. Kavanaugh, L. W. Juranek, and R. A. Feely. 2012. High-resolution estimates of net community production and air-sea CO_2 flux in the northeast Pacific. Global Biogeochem. Cycles **26**. doi:10.1029/2012GB004380

Manning, C. C., R. H. R. Stanley, and D. E. Lott. 2016. Continuous Measurements of Dissolved Ne, Ar, Kr, and Xe Ratios with a Field-Deployable Gas Equilibration Mass Spectrometer. Anal. Chem. **88**: 3040–3048. doi:10.1021/acs.analchem.5b03102

Mathis, J. T., N. R. Bates, D. A. Hansell, and T. Babila. 2009. Net community production in the northeastern Chukchi Sea. Deep Sea Res. Part II Top. Stud. Oceanogr. **56**: 1213–1222.

doi:10.1016/j.dsr2.2008.10.017

McNeil, C. L., B. D. Johnson, and D. M. Farmer. 1995. In-situ measurement of dissolved nitrogen and oxygen in the ocean. Deep. Res. Part I **42**: 819–826. doi:10.1016/0967-0637(95)97829-W

McNeil, C. L., D. Katz, R. Wanninkhof, and B. Johnson. 2005. Continuous shipboard sampling of gas tension, oxygen and nitrogen. Deep. Res. Part I Oceanogr. Res. Pap. **52**: 1767–1785. doi:10.1016/j.dsr.2005.04.003

Mesinger, F., G. DiMego, E. Kalnay, and others. 2006. North American Regional Reanalysis. Bull. Am. Meteorol. Soc. **87**: 343–360. doi:10.1175/BAMS-87-3-343

Mordy, C. W., S. Bell, E. D. Cokelet, and others. 2020. Seasonal and interannual variability of nitrate in the eastern Chukchi Sea: Transport and winter replenishment. Deep. Res. Part II Top. Stud. Oceanogr. **177**: 104807. doi:10.1016/j.dsr2.2020.104807

Mordy, C. W., L. Eisner, K. Kearney, and others. 2021. Spatiotemporal variability of the nitrogen deficit in bottom waters on the eastern Bering Sea shelf. Cont. Shelf Res. **224**: 104423. doi:10.1016/j.csr.2021.104423

NASA Goddard Space Flight Group; Ocean Ecology Laboratory; Ocean Biology Processing Group. Moderate-resolution Imaging Spectroradiometer (MODIS) Aqua Chlorophyll Data; 2018 Reprocessing. NASA OB.DAAC, Greenbelt, MD, USA. doi:data/10.5067/AQUA/MODIS/L3M/CHL/2018

Padin, X. A., M. Vázquez-Rodríguez, A. F. Rios, and F. F. Pérez. 2007. Atmospheric CO2 measurements and error analysis on seasonal air-sea CO2 fluxes in the Bay of Biscay. J. Mar. Syst. **66**: 285–296. doi:10.1016/j.jmarsys.2006.05.010

Quay, P., J. Stutsman, and T. Steinhoff. 2012. Primary production and carbon export rates across the subpolar N. Atlantic Ocean basin based on triple oxygen isotope and dissolved O 2 and Ar gas measurements. Global Biogeochem. Cycles **26**: 1–13. doi:10.1029/2010GB004003

Reuer, M. K., B. A. Barnett, M. L. Bender, P. G. Falkowski, and M. B. Hendricks. 2007. New estimates of Southern Ocean biological production rates from O2/Ar ratios and the triple isotope composition of O2. Deep Sea Res. Part I Oceanogr. Res. Pap. **54**: 951–974. doi:10.1016/j.dsr.2007.02.007

Semiletov, I., A. Makshtas, S.-I. Akasofu, and E. L Andreas. 2004. Atmospheric CO 2 balance: The role of Arctic sea ice. Geophys. Res. Lett. **31**: n/a-n/a. doi:10.1029/2003GL017996

Serreze, M. C., and J. Stroeve. 2015. Arctic sea ice trends, variability and implications for seasonal ice forecasting. Philos. Trans. R. Soc. A Math. Phys. Eng. Sci. **373**. doi:10.1098/rsta.2014.0159

Shadwick, E. H., B. Tilbrook, N. Cassar, T. W. Trull, and S. R. Rintoul. 2015. Summertime physical and biological controls on O2 and CO2 in the Australian Sector of the Southern Ocean. J. Mar. Syst. **147**: 21–28. doi:10.1016/j.jmarsys.2013.12.008

Shiozaki, T., A. Fujiwara, M. Ijichi, N. Harada, S. Nishino, S. Nishi, T. Nagata, and K. Hamasaki. 2018. Diazotroph community structure and the role of nitrogen fixation in the nitrogen cycle in the Chukchi Sea (western Arctic Ocean). Limnol. Oceanogr. **63**: 2191–2205. doi:10.1002/lno.10933

Song, H., R. Ji, M. Jin, Y. Li, Z. Feng, Ø. Varpe, and C. S. Davis. 2021. Strong and regionally distinct links between ice-retreat timing and phytoplankton production in the Arctic Ocean. Limnol. Oceanogr. 1–11. doi:10.1002/lno.11768

Stammerjohn, S., R. Massom, D. Rind, and D. Martinson. 2012. Regions of rapid sea ice change : An inter-hemispheric seasonal comparison. **39**: 1–8. doi:10.1029/2012GL050874

Stanley, R. H. R., J. B. Kirkpatrick, N. Cassar, B. A. Barnett, and M. L. Bender. 2010. Net community production and gross primary production rates in the western equatorial Pacific. Global Biogeochem. Cycles **24**. doi:10.1029/2009GB003651

Stroeve, J., and W. N. Meier. 2018. Sea Ice Trends and Climatologies from SMMR and SSM/I-SSMIS, Version 3.doi:10.5067/IJ0T7HFHB9Y6

Teeter, L., R. C. Hamme, D. Ianson, and L. Bianucci. 2018. Accurate Estimation of Net Community Production From O2/Ar Measurements. Global Biogeochem. Cycles **32**: 1163–1181. doi:10.1029/2017GB005874

Thomson, J., and W. E. Rogers. 2014. Swell and sea in the emerging Arctic Ocean. Geophys. Res. Lett. **41**: 3136–3140. doi:10.1002/2014GL059983

Toole, J. M., M. L. Timmermans, D. K. Perovich, R. A. Krishfield, A. Proshutinsky, and J. A. Richter-Menge. 2010. Influences of the ocean surface mixed layer and thermohaline stratification on Arctic Sea ice in the central Canada Basin. J. Geophys. Res. Ocean. **115**: 1–14. doi:10.1029/2009JC005660

Tremblay, J.-É., and J. Gagnon. 2009. The effects of irradiance and nutrient supply on the productivity of Arctic waters: a perspective on climate change. Influ. Clim. Chang. Chang. Arct. Sub-Arctic Cond. 73–93. doi:10.1007/978-1-4020-9460-6_7

Tremblay, J. É., L. G. Anderson, P. Matrai, P. Coupel, S. Bélanger, C. Michel, and M. Reigstad. 2015. Global and regional drivers of nutrient supply, primary production and CO2 drawdown in the changing Arctic Ocean. Prog. Oceanogr. **139**: 171–196.

doi:10.1016/j.pocean.2015.08.009

Tremblay, J. É., S. Bélanger, D. G. Barber, and others. 2011. Climate forcing multiplies biological productivity in the coastal Arctic Ocean. Geophys. Res. Lett. **38**: 2–6. doi:10.1029/2011GL048825

Trull, T. W., P. Jansen, E. Schulz, B. Weeding, D. M. Davies, and S. G. Bray. 2019. Autonomous Multi-Trophic Observations of Productivity and Export at the Australian Southern Ocean Time Series (SOTS) Reveal Sequential Mechanisms of Physical-Biological Coupling. Front. Mar. Sci. **6**: 1–17. doi:10.3389/fmars.2019.00525

Wanninkhof, R. 2014. Relationship between wind speed and gas exchange over the ocean revisited. Limnol. Oceanogr. Methods **12**: 351–362. doi:10.4319/lom.2014.12.351

Wassmann, P., and M. Reigstad. 2011. Future Arctic Ocean Seasonal Ice Zones and Implications for Pelagic-Benthic Coupling. Oceanography **24**: 220–231. doi:10.5670/oceanog.2011.74

Weeding, B., and T. W. Trull. 2014. Hourly oxygen and total gas tension measurements at the Southern Ocean Time Series site reveal winter ventilation and spring net community production. J. Geophys. Res. Ocean. **119**: 348–358. doi:10.1002/2013JC009302

Weiss, R. F., and B. A. Price. 1980. Nitrous oxide solubility in water and seawater. Mar. Chem. **8**: 347–359. doi:10.1016/0304-4203(80)90024-9

Woolf, D. K., and S. A. Thorpe. 1991. Bubbles and the air-sea exchange of gases in near-saturation conditions. J. Mar. Res. **49**: 435–466. doi:10.1357/002224091784995765